

The First Spatially Resolved Mid-IR Spectra of NGC 1068 Obtained at Diffraction-limited Resolution with LWS at Keck I Telescope

JOSEPH H. RHEE

`jrhee@gemini.edu`

Gemini Observatory, 670 N. A'ohoku Place, Hilo, HI 96720

JAMES E. LARKIN

`larkin@astro.ucla.edu`

Dept. of Physics and Astronomy, University of California, Los Angeles

ABSTRACT

We present spatially resolved mid-IR spectra of NGC 1068 with a diffraction-limited resolution of $0.25''$ using the Long Wavelength Spectrometer (LWS) at the Keck I telescope. The mid-infrared image of NGC 1068 is extended along the N-S direction. Previous imaging studies have shown the extended regions are located inside the ionization cones indicating that the mid-infrared emission arises perhaps from the inner regions of the narrow-line clouds instead of the proposed dusty torus itself. The spatially resolved mid-IR spectra were obtained at two different slit position angles, $+8.0$ and -13.0 degrees across the elongated regions in the mid-IR. From these spectra, we found only weak silicate absorption toward the northern extended regions but strong in the nucleus and the southern extended regions. This is consistent with a model of a slightly inclined cold obscuring torus which covers much of the southern regions but is behind the northern extension. While a detailed analysis of the spectra requires a radiative transfer model, the lack of silicate emission from the northern extended regions prompts us to consider a dual dust population model as one of the possible explanations in which a different dust population exists in the ionization cones compared to that in the dusty torus. Dust inside the ionization cones may lack small silicate grains giving rise to only a featureless continuum in the northern extended regions while dust in the dusty torus has plenty of small silicate grains to produce the strong silicate absorption lines towards the nucleus and the southern extended regions.

Subject headings: Infrared Spectroscopy, Seyferts, Active Galactic Nuclei: individual(NGC 1068

1. Introduction

AGNs appear in a variety of types, which are often classified based on the presence of broad emission lines. Objects are classified as type I if both broad and narrow emission lines appear in their optical spectra and as type II if only narrow emission lines are present without broad emission lines. It is, however, a general belief that much of the observed diversity in the local universe arises from different viewing angles toward the central engine and a dusty toroidal structure around it, especially for Seyfert galaxies of types I and II. When the dusty torus is viewed face-on, both the central engine and the broad-line regions can be seen directly causing objects to appear as Seyfert 1 galaxies. When the dusty torus is viewed edge-on, the anisotropic obscuration created by the torus causes objects to appear as Seyfert 2 galaxies (see Antonucci 1993 for review). It is this crucial role played by dust in the Unified model of AGN that makes understanding dust properties very important in understanding AGN.

A significant fraction of the optical/UV/X-ray luminosity of the active nucleus is absorbed by the proposed dusty torus and reradiated at mid-infrared wavelengths. The infrared also suffers less extinction than the optical band and is preferred for probing the proposed dusty torus or dust in general in the nucleus. Early mid-infrared observations of Seyfert galaxies (Roche et al. 1991) have shown that the $9.7 \mu\text{m}$ silicate feature appears in strong absorption in Seyfert 2's as expected from an edge-on geometry of the proposed dusty torus for type II objects. If the dust responsible for the $9.7 \mu\text{m}$ silicate feature belongs to the dusty torus, then the spatial distribution of the silicate absorption can provide very important clues to the physical properties (size, orientation, etc.) of the dusty torus.

It is, however, difficult to investigate the spatial distribution of dust in Seyfert galaxies because mid-IR emission from most Seyfert galaxies has not been resolved (see Gorjian et al. 2004). While thermal emission from hot dust has been considered as a dominant source of the mid-IR emission of Seyfert galaxies, the unresolved nature of the mid-IR image have left the discussion over a non-thermal origin still alive. NGC 1068 is one of a few Seyfert galaxies whose mid-IR emission is resolved. No other alternative mechanism like synchrotron radiation can produce emission over such an extended area, leaving heated dust grains as the likely source.

NGC 1068 is classified as a Seyfert 2 based on the presence of narrow emission lines and absence of broad emission lines. The detection of broad emission lines in polarized light (Antonucci and Miller 1985), however, has shown that NGC 1068 harbors an obscured Seyfert 1 nucleus. As one of the closest and brightest Seyfert 2 galaxies, NGC 1068 offers a better spatial scale for the detail investigation of its obscured nucleus. NGC 1068 is at 14.4 Mpc (Tully 1998) so $1''$ corresponds to 72 pc or $0.25''$ (our spatial resolution) corresponds to 18 pc in physical distance. As a part of a greater mid-infrared survey of a sample of Seyfert galaxies, NGC 1068 was selected specifically for the investigation of the physical properties of the proposed dusty torus.

NGC 1068 has been observed many times in the mid-infrared both in imaging and spectroscopic modes. The spatially resolved mid-IR images of NGC 1068 show a linear structure covering about $1''$ in the north-south direction (Braatz et al. 1993; Cameron et al. 1993; Bock et al. 2000; Tomono et al. 2001). Emission line imaging of O[III] showed that this disklike structure lies inside the narrow-line regions (Evans et al. 1991; Macchetto et al. 1994). Since the narrow-line regions are believed to be created by the ionizing radiation from the central engine which is collimated by the dust torus, the dusty torus should be oriented in the East-West direction perpendicular to the narrow-line cones. Thus this structure has been believed to be created by grains in the NLRs heated by the nuclear radiation. In this model, the dusty torus is then too cold to emit significantly at $10\ \mu\text{m}$.

While recent mid-infrared imaging studies have provided some spatially resolved dust measurements in the nuclear region of NGC 1068, no spatially resolved spectra have been obtained in the mid-infrared until this study. Mid-infrared spectra of NGC 1068 have also been obtained repeatedly by several single aperture ground-based telescopes and Infrared Space Observatory (ISO) using various apertures from $0.4''$ at VLTI to $24'' \times 24''$ at ISO (Lutz et al. 2000; Le Floch et al. 2001; Jaffe et al. 2004; Roche et al. 1991; Siebenmorgen, Krugel, and Spoon 2004). Most previous spectra show that the mid-infrared spectra of NGC 1068 have significant silicate absorption. Especially Sturm et al. (2000) and Lutz et al. (2000) show the AGN dominated spectra with no significant PAH emission lines.

A crude spatial map of the distribution of the silicate absorption has been provided by imaging studies using multiple narrow bands, most notably from Bock et al. (2000) and Galliano et al. (2003). However, these studies have given conflicting results making spatially resolved spectra necessary to resolve the issues. For example, Bock et al. (2000) has reported that the silicate feature is relatively strong in absorption on the nucleus and to the south but flat or even in emission to the north. In contrast, Galliano et al. (2003) found that the silicate feature appears strong in absorption to the north but either flatter or in emission to the south. For the first time, we present the diffraction-limited mid-infrared

spectra of NGC 1068 at a spatial resolution of $0.25''$ to investigate the spatial distribution and the properties of dust in the nuclear regions.

2. Observation & Data Reduction

The mid-infrared spectra of NGC 1068 were obtained on September 6th, 2003 as a part of a larger mid-infrared spectroscopic survey of nearby Seyfert galaxies. The low-resolution spectroscopic mode of the Long Wavelength Spectrograph (LWS; Jones & Puetter 1993) was used at the f/25 forward Cassegrain focus of the Keck I 10 m telescope. LWS uses a 128 x 128 pixel Boeing Si:As array with a spatial pixel scale of $0.08''$. For the present spectra, a slit with a 3 pixel width was used in the bottom $3.6''$ (45 pixels) of the array giving a $0.24''$ by $3.6''$ of slit size. The spectral dispersion is $0.0375 \mu\text{m}$ per pixel. The N-wide filter with a central wavelength of $10.1 \mu\text{m}$ was selected to give wavelength coverage of $7.71 - 12.48 \mu\text{m}$. This wavelength range includes prominent PAH emission lines at $8.6 \mu\text{m}$ and $11.3 \mu\text{m}$ as well as a wide silicate absorption line at $9.7 \mu\text{m}$.

A log of our observations is presented in Table 1. The observations were made under excellent atmospheric conditions with low water vapor. Air masses varied between 1.06 and 1.11. The telluric absorption was measured by observing several standard stars, HR 337, HR 617, HR 8781, and HR 1017. The spectra of NGC 1068 were obtained at three different slit position angles, $+8.0$, $+78.9$, and -13.0 degrees which were selected based on both the direction of the extended mid-infrared core and the location of bright guide stars. In LWS, the slit position angle on the sky is determined by the location of a bright offset guide star, which controls the telescope tracking. The guide star for the slit position angles of $+8.0^\circ$ and -13.0° were bright enough to give stable tracking. But the guide star at $+78.9^\circ$ was not bright enough so tip-tilting errors were visible.

The standard “chop-nod” mode was used in the observation in order to suppress sky emission and radiation from the telescope. The field was chopped at a frequency of 2 Hz and nodded every 30 sec. The chopping and nod directions were set to the same direction, parallel to the slit. The nodding amplitude was the same as the chopping amplitude of $10''$. An individual spectrum set was created by coadding a total of 60 frames with 50 ms integration time at each chop beam. These individual sets were then combined to produce 7 nodsets per each runtime with total on-source integration time of 168 sec. Three runtime spectra were acquired at each slit position angle for NGC 1068.

The raw spectra for both NGC 1068 and the standard stars were first sky-subtracted using the sky frame of the chop pair and flat-fielded. Bad pixels were replaced by the

median of their neighboring pixels. The resultant spectra were then spatially rectified by a first order polynomial before shifting the images parallel to the slit to align the peak position and in the direction of dispersion to align atmospheric absorption lines. After combining the images from each runtime set, a wavelength calibration was applied to them using atmospheric transmission lines¹ with wavelengths calculated by Lord (1992).

The average spectrum of 4 standard stars was divided by a simulated blackbody spectrum with the star’s effective temperature and then divided into each runtime spectrum of NGC 1068 in order to remove atmospheric and instrumental features including the deep ozone absorption band at $9.6 \mu\text{m}$. HR 1017, a F5 star, was observed closest in time to NGC 1068 but at a worse airmass, 1.17. After many trials, we found that the average spectrum of all four standard stars yielded the best telluric correction in the spectra of NGC 1068. The upper panel of Figure 1 shows the mid-infrared spectra of NGC 1068 at the nucleus divided by the spectrum of either HR 1017 or the average of 4 standard stars. The bottom panel displays the average spectrum of all 4 standard stars as well as their individual spectrum. When divided by the average spectrum, the spectrum of NGC 1068 looks much smoother in the short wavelength regions between $8.0\mu\text{m}$ and $9.3\mu\text{m}$.

Before extracting the one-dimensional spectra of NGC 1068, 14 individual chop sets in each runtime set were inspected in order to check whether the seeing was stable throughout the exposure. Although three runtime sets were acquired at each position angle, only one runtime set was found to be stable at the slit position angles of $+8.0^\circ$ and -13.0° . Thus one-dimensional spatially-resolved spectra were obtained by extracting consecutive 3 rows ($0.25''$) in the spatial direction from the maximum emission of the single stable runtime set. For the total slit spectra, total 24 rows ($2''$) were combined to produce 1-D spectra from the average of 3 runtime sets.

Once the 1-D spectra were extracted for each galaxy, we used a foreground screen model consisting of a power law continuum and silicate absorption line to fit the observed silicate feature. The silicate extinction curve was produced by Dudley and Wynn-Williams (1997) using the μ Cep emissivity curve given by Roche and Aitken (1984). We used four free parameters for the fitting: the amplitude of the power law; a power-law index, s , for $F_\lambda \sim \lambda^s$; a visual extinction, A_v ; and the central wavelength, λ_c . We excluded the wavelength regions of strong atmospheric contamination and [SIV] emission ($\lambda = 10.511 \mu\text{m}$ in the rest frame) and came up with the three wavelength intervals, $8.2 - 9.2 \mu\text{m}$, $9.8 - 10.4$, $10.6 - 12.4 \mu\text{m}$ that were used for the fit (Figure 1). The silicate absorption profile was redshifted to

¹The actual data set of the atmospheric transmission lines were obtained from the website of the Gemini Observatory.

match the observed spectra before the fitting process. We began with a very rough power-law fit to estimate the initial amplitude and the slope. We also get a rough estimate of the visual extinction and the central wavelength by eye. Then we ran a grid search to find a best fit to the observed spectrum. First, we started the search within ± 40 per cent of the initial values for the first 3 parameters in 1 per cent increments. For the central wavelength, the iteration was run within $\pm 2 \mu\text{m}$ from the best guessed central wavelength in $0.1 \mu\text{m}$ increment. Then from the best fit result of the initial search, we ran the grid search again with a 0.1 percent increment within ± 20 per cent of the revised center. Most times the fit converged but sometimes it did not. Once the best fit was obtained, we measured the calculated Chi Square (χ^2/N) using the same three intervals that we used for the fitting to obtain the standard deviation of our spectra. The noise of our mid-infrared data is background limited and does not vary much outside the spectral region contaminated by atmospheric absorption. Three spectra with χ^2/N under unity suggest that the reduced Chi Square value is perhaps underestimated by an overestimation of the noise in the spectra.

3. Results

The mid-infrared spectra of NGC 1068 were obtained at 3 different slit position angles, slit PA = $+8^\circ$, $+78.9^\circ$, and -13° . The spectra along $+8^\circ$ and -13° slits were spatially resolved along the N-S elongated regions while the spectrum along $+78.9^\circ$ slit was not extended. We present diffraction-limited total integrated fluxes along each slit position in Figure 2. The observed data are shown in a solid line while the fit with the silicate extinction profile as a dashed line in each figure. For the spectra along $+8^\circ$ and -13° slits, we also display the relative flux from the central $0.25'' \times 0.25''$ rectangular region (Central Engine, CE) in the same figures for comparison. In each slit, the flux from CE accounts for a little more than a quarter of the total flux. As mentioned in the previous section, the spectrum along the $+78.9^\circ$ slit is noisier than the other two spectra due to a notable tracking problem from using a faint guide star. The two spectra along the N-S elongated regions look very similar to each other. They both have similar slopes and show significant silicate absorption (Figures 2a and 2b). But the spectrum perpendicular to the N-S elongated regions looks steeper and has less silicate absorption than the others (Figure 2c).

Overall the mid-infrared spectra of NGC 1068 are dominated by the broad silicate absorption line without strong emission features. Although not strong, [S IV] emission lines are apparent in all 3 spectra. We found that the silicate absorption lines are fit better with a small shift of the silicate absorption center. Given that the spectral resolution of our data is $0.11 \mu\text{m}$, the shift is marginal ($\Delta\lambda \lesssim 2 \sigma$). The shifts may, however, be real as they all

occur toward the shorter wavelength (see Table 2). Sturm et al. (2000) have reported a more significant shift in the broad silicate absorption feature centered at $9.4 \mu\text{m}$ in their ISO-SWS spectra of NGC 1068. But it was suspected that the contamination by the large ISO beam (various apertures between $14'' \times 20''$ and $20'' \times 33''$) might have caused the apparent blue shift of the silicate absorption center (Bock et al. 2000).

In Figure 3, we display our mid-IR spectrum (Keck LWS) and the UKIRT spectrum (Roche et al. 1991) on top of the ISO-SWS spectrum (Lutz et al. 2000) of NGC 1068. For our spectrum in Figure 3, two spectra along $+8^\circ$ and -13° slits were averaged together and scaled to match the flux of the ISO-SWS spectrum. The UKIRT spectrum is a reproduction of the mid-infrared spectrum of NGC 1068 in Figure 1 from Roche et al. (1991). λF_λ was first converted to F_ν and then scaled to match the ISO-SWS spectrum.² Our spectrum matches both the UKIRT spectrum and the ISO-SWS spectrum quite well in both the depth and the slope of the silicate absorption feature although each spectrum depicts a very different physical scale. Our Keck LWS spectrum represents central $0.25'' \times 2''$ ($18 \text{ pc} \times 140 \text{ pc}$ in physical scale) while the UKIRT spectrum serves about 3 times and the ISO-SWS spectrum about 10 times bigger areas in NGC 1068. In general, the mid-IR spectra of Seyfert 2 galaxies obtained with a large aperture show very different features than those with a small aperture. For example, an average ISO spectrum of 27 Seyfert 2 galaxies shows that strong PAH emission lines dominate the mid-IR regions (Clavel et al. 2000) due to contamination from host galaxy light. But the mid-IR spectra taken with small apertures display a significant silicate absorption feature without strong PAH emission lines (Siebenmorgen, Krugel, and Spoon 2004; Soifer et al. 2002, see Rhee and Larkin 2005 for further discussion). A better spatial resolution of NGC 1068 resulted from its proximity may explain why AGN in NGC 1068 dominates both the ISO-SWS and other small aperture spectra revealing a significant silicate absorption without strong PAH emission lines. In their ISO-CAM image of NGC 1068 (Figure 2b), Le Floc’h et al. (2001) shows that in NGC 1068 PAH feature at $7.7 \mu\text{m}$ is very weak within $\sim 10''$ circular radius from the nucleus but gets stronger further out and peaks around $15''$ away from the nucleus. If NGC 1068 were located at ~ 20 parsec from the Earth as other typical Seyfert 2’s, the ISO-SWS spectrum would have easily included strong PAH features.

Our mid-IR spectrum (Keck LWS) as well as the UKIRT spectrum and the ISO-SWS spectrum shows, however, a stronger silicate absorption than ISO CAM-CVF spectrum of the nucleus of NGC 1068 does (see Figure 4 in Le Floc’h et al. 2001). Applying the same

²The actual data from Roche et al. (1991) has $\sim 15\%$ less flux than what is shown in Figure 1. The additional flux in ISO-SWS spectrum may come from its larger aperture. The overall shape and the strength of the silicate feature of both spectra, however, agree with each other well.

screen model from Dudley and Wynn-Williams (1997), we found $A_v \sim 10$ mag while Le Floch et al. (2001) reported $A_v \sim 7$ mag. It is not clear why ISO CAM-CVF spectrum shows a flatter and less significant silicate absorption in the nucleus of NGC 1068. Rieke and Low (1975) has also reported a weak silicate absorption in NGC 1068. Their infrared spectrum of NGC 1068 was not, however, acquired from a spectroscopic observation but inferred from several narrow-band photometry results. As discussed further in section 4, such a spectrum does not necessarily agree with the spectroscopic data.

For the $+8^\circ$ and -13° slit PA's, we extracted spectra from 8 regions along the slit: four positions from the northern extended region, one position at the nucleus, and three positions from the southern extended region. Each spectrum represents the spectrum in a square beam of $0.25'' \times 0.25''$. In Figures 4 and 5, we overlay each slit on top of the $12.5 \mu\text{m}$ image by Bock et al. (2000) and present all 8 spectra along each slit. Centered on the nucleus, the slit along $+8^\circ$ crosses most of the northern extended region, all the way through the upper tongue in the north-east tip of the extended image. In the south, the slit along $+8^\circ$, however, misses the bright south-east spot. The slit along -13° covers the most extended regions well from the southern bright spot to the northern bright spot except the upper tongue in the north-east. Figures 4 and 5 show that the spectra on the nucleus are bluer but get steeper away from the nucleus indicating that the mid-infrared continuum in the nucleus is dominated by hotter dust than dust off the nucleus. The [S IV] emission line appears in all the extended regions and the relative strength increases with the distance away from the central engine.

The strength of the silicate absorption varies over the extended regions. It is strongest on the nucleus and declines to the north. This trend shows that our line of sight transmits through the largest amount of the cold dust toward the nucleus and intercepts less cold dust off from the nucleus. In addition, the silicate absorption remains relatively strong in the southern extended region but declines fast in the northern extended region as noted by Bock et al. (2000). This asymmetry may result from the northern opening of the torus being slightly tilted toward our line of sight. No silicate emission was detected in any region, contrasting previous studies which had hinted at silicate line emission in the northern extended regions (Bock et al. 2000) or in the southern extended regions (Galliano et al. 2003). This is discussed further in section 4.

In the appendix, we display individual spectra along each slit position in Figures 9 thru 15 with brief explanations in the text. Each observed spectrum is represented by a solid line along with the best silicate extinction fit shown as a dashed line. In general, the fits are reasonable ($\chi^2/N \lesssim 2.0$) except in the spectral regions contaminated by strong atmospheric absorption lines (i.e. $\lesssim 8 \mu\text{m}$ and $9.2 \mu\text{m} \sim 9.7 \mu\text{m}$). Table 2 summarizes parameters

used to fit each individual spectrum. As discussed further in Sect. 4, the bestfit parameters, especially A_v , should be taken with a caution as the cold screen model may not apply to all the regions, especially in the north.

4. Discussion

Previous imaging studies have produced local mid-infrared SEDs and estimates of the silicate absorption by combining spatially resolved narrow-band fluxes. Both Bock et al. (2000) and Galliano et al. (2003) provide such SEDs which don't agree with each other. In the northern extended regions, Bock et al. (2000) show no silicate absorption but a smooth continuum, perhaps even silicate in emission. On the other hand, Galliano et al. (2003) find the silicate feature in absorption with a depth that increases with the distance from the central engine (CE). Our results do not, however, agree with either of the results above. Our spectra show that the silicate feature appears weak in absorption in the northern extended regions and with its depth decreasing with distance from the CE instead of increasing suggested by Galliano et al. (2003). In the southern extended regions, our spectra show significant silicate absorption in the southern extended regions consistent with that of Bock et al. (2000).

We believe such discrepancies arise because their local SED were synthesized from individual narrow-band images observed at different times and may suffer variable seeing conditions. Under different seeing conditions, it is hard to compare accurately the fluxes of different bands. Our spectra do not, however, suffer from such uncertainty as all 8 positions within an individual N-band spectra were obtained simultaneously.

The presence of the prominent structure to the north in the mid-infrared image was used to indicate that the north axis of the torus opening is tilted towards our line of sight (Bock et al. 2000). The presence of strong silicate absorption towards the southern extended region supports this picture as it indicates obscuration from optically thick dust grains in the south. However, the presence of weak silicate absorption to the north is interesting. If we assume a simple torus model in which the northern opening is oriented towards us, then we might expect to see hot dust on the inner edge in emission assuming a similar dust composition as the obscuring material. We may not, however, have the same kind of cold foreground screen toward the hot diffuse dust in the north as to the nucleus and the south; thus, it is difficult to draw any firm conclusion by applying the same model to all regions and comparing the strength of the silicate features quantitatively based on the model fit such as the visual extinctions, A_v . A radiative transfer model is required to address properly the apparent differences in the strength of the silicate feature at various locations because

dust temperature distribution and geometric effect affect the silicate feature amplitude. For non-spatially resolved mid-IR spectra of NGC 1068, many theoretical works have already been done using various radiative transfer models over last a couple of decades (Pier and Krolik 1992, 1993; Granato and Danese 1994; Granato, Danese, and Franceschini 1997; Rowan-Robinson 1995; Nenkova, Ivezić, and Elitzur 2002).

In the absence of a radiative transfer model, one may still speculate a depletion of small grains within the elongated extended regions as one of the possibilities to explain the observed spectra in the north. The possible depletion of small grains in the AGN environment has been suggested by various authors (Maiolino et al. 2001; Weingartner and Murray 2001; Rhee and Larkin 2005). The fact that the northern extended regions reside inside the ionization cone renders further speculation. The formation of the ionization cone in NGC 1068 is discussed in three different ways by Bock et al. (2000): Relativistic beaming, Dust absorption, and Electron scattering. In all three ways, the dust grains inside the ionization cones are directly heated by very strong UV radiation from the nuclear engine. This direct heating and other processes in the cone can destroy small grains. Figure 6 shows that only small grains less than $3 \mu\text{m}$ effectively give rise to the silicate feature seen in the mid-infrared spectra of Seyfert galaxies. The effective destruction of small grains by strong nuclear radiation may explain the observed lack of silicate emission from the northern extended regions. The weak silicate absorption in the northern extended regions could be created due to absorption by cold dust grains puffed up from the torus between the observer and the hot dust grains that emit the continuum.

In contrast, the small grains in the cold outer regions of the dusty torus are shielded from and therefore survive the intense UV radiation. These small silicate grains can effectively absorb the continuum and create the silicate absorption feature observed in the mid-infrared spectra of NGC 1068. Our spectra show that silicate absorption remains strong even to the location South 3. If the silicate grains responsible for the apparent silicate absorption belong to the dusty torus, this indicates that the dusty torus should extend at least tens of parsecs in vertical direction. A recent interferometric mid-infrared observation of NGC 1068, however, has revealed a parsec scale structure believed to be the dusty torus (Jaffe et al. 2004). Perhaps the outer cold regions of a dusty torus do not radiate significantly at $10 \mu\text{m}$ because they are too cold. The parsec structure found in the interferometric image most likely come from the heated inner regions of the dusty torus because the interferometric mid-infrared spectra indicate the presence of cold small grains in the foreground by showing deep silicate absorption. It is perhaps that the outer radius of the torus reaches out to more than tens of parsec. The dust distribution in the nuclear environment of NGC 1068 is summarized in Figure 7.

5. Summary and Conclusions

We used the Long Wavelength Spectrometer (LWS) at Keck I telescope with a $0.25''$ slit to obtain spatially-resolved spectra of NGC 1068 at three different slit positions, slit PA = $+8^\circ$, -13° , and $+78.9^\circ$. Overall our integrated spectra agrees with the previous mid-IR spectra well. In NGC 1068, our resolved spectra showed that the silicate absorption was strongest on the nucleus (Central Engine) indicating that our line of sight transmitted through the largest amount of cold obscuring dust materials to the nucleus. Furthermore, the strength of the silicate absorption declines fast to the north but remains relatively strong to the south. This asymmetry in the strength of the silicate absorption as well as the larger extended emission regions to the north suggests that the north pole of the torus opening is inclined towards us and that the southern extended regions are behind the obscuring dusty torus. Based on the lack of strong silicate emission from the north, we considered the dual dust population model for AGN in which two different dust populations exist in the ionization cones and in the dusty torus. The dust population in the ionization cones may lack small silicate grains or small grains in general and give rise to featureless continuum to the north while the dust population in the dusty torus contains plenty of small silicate grains and causes the apparent deep silicate absorption lines to the nucleus and the south in NGC 1068. A detailed analysis using a radiative transfer model would provide a better understanding to our spatially resolved mid-IR spectra.

We like to thank Randy Campbell for support during the observation with LWS at Keck I telescope. We thank Chris Dudley at Naval Observatory for his valuable comments as well as the cold screen model of the $9.7 \mu\text{m}$ silicate absorption feature used in this paper. We appreciate Dieter Lutz and Pat Roche for their ISO-SWS and UKIRT spectra reproduced Figure 3. Jamie J. Bock also kindly provided the images of NGC 1068 reproduced in Figures 4 and 5. We are grateful to Aigen Li for providing the code to produce Figure 6. We acknowledge useful conversations with Ari Laor, Matt Malkan and Eric Becklin. J.R. thanks K. Cha and I. Song for their help in creating Figure 7.

A. Appendix material

A.1. Mid-IR spectra at the Central Engine

Figure 8 depicts the nuclear spectra of NGC 1068 at the central $0.25'' \times 0.25''$ location (Central Engine, CE) along the $+8^\circ$ slit in the top panel and the -13° slit in the bottom panel. Produced essentially from the same region, they look almost identical except at

different relative flux levels. The spectra at the central engine is the strongest overall and contain at least one-quarter of the total flux in the slit (see Figure 2). The spectra at the central engine rises at the short wavelength end indicating that the nuclear flux at the mid-infrared is dominated by hotter dust than dust off the nucleus. The silicate absorption is also strongest here implying the line of sight transmits through the largest amount of cold silicate grains. The silicate absorption line is best fit with the silicate extinction profile whose centers fall on $9.57 \mu\text{m}$ in the top panel and $9.60 \mu\text{m}$ in the bottom panel instead of $9.7 \mu\text{m}$. A weak [S IV] emission line appears at $10.5 \mu\text{m}$ in both spectra.

A.2. Mid-IR spectra at North 1

Figure 9, North 1, shows the spectra of NGC 1068 at $0.25''$ off the central peak to the north along the $+8^\circ$ slit in the top panel and the -13° slit in the bottom panel. Overall they look similar to each other. Flux decreases significantly to about one half of the CE and the spectra are much steeper. The silicate absorption is still significant but greatly reduced compared to the CE and even to South 1. Figure 9 shows that the silicate extinction profile fits the observed data extremely well at both slit positions. The best fit centers of the silicate absorption lines are to the blue of the nominal wavelength in both panels. The [S IV] emission lines have a larger equivalent width than at the CE and appear at $10.5 \mu\text{m}$ in both spectra.

A.3. Mid-IR spectra at North 2

Figure 10, North 2, shows the spectra of NGC 1068 at $0.50''$ north of the central peak along the $+8^\circ$ slit in the top panel and the -13° slit in the bottom panel. In both panels, the spectra appear almost flat with weak silicate absorption in the middle. The flux drops to around 30% of the CE. The silicate extinction curve fit continues to match the observed data well with its center shifted to $9.54 \mu\text{m}$ in both the top and bottom panels.

A.4. Mid-IR spectra at North 3

Figure 11, North 3, shows the spectra of NGC 1068 at $0.75''$ off the central peak to the north along the $+8^\circ$ slit in the top panel and the -13° slit in the bottom panel. The spectrum in the top panel (from the $+8^\circ$ slit) is approximately centered on the $12 \mu\text{m}$ feature called the “tongue”, which is to the North-north-east of the nucleus. In both spectra, the flux is

around 5% of the CE. The silicate absorption continues to appear weak while the relative [S IV] emission is stronger than in North 2.

A.5. Mid-IR spectra at North 4

Figure 12, North 4, depicts the spectra of NGC 1068 at $1.0''$ off the central peak to the north along the $+8^\circ$ slit in the top panel and the -13° slit in the bottom panel. Both spectra have low fluxes and appear noisy as they represent the regions outside the contours on the $12\ \mu\text{m}$ map. The spectra rise toward the long wavelength. The [S IV] equivalent width is stronger than at any other region except South 3 along the -13° slit.

A.6. Mid-IR spectra at South 1

Figure 13, South 1, depicts the spectra of NGC 1068 at $0.25''$ south of the central peak along the $+8^\circ$ slit in the top panel and the -13° slit in the bottom panel. Even with a substantial decline in flux, the silicate absorption at South 1 remains as strong as in the CE contrary to North 1 in which the silicate absorption drops significantly, indicating that a large amount of obscuring cold dust still remains in the foreground. Here the amount of the shift in the centers of the silicate absorption lines in both panels are least among all the regions. The [S IV] equivalent width appears as weak as at the CE.

A.7. Mid-IR spectra at South 2

Figure 14, South 2, depicts the spectra of NGC 1068 at $0.50''$ south of the central peak along the $+8^\circ$ slit in the top panel and the -13° slit in the bottom panel. The bottom spectrum presented in South 2 along the -13° slit is from the southern bright knot in the $12\ \mu\text{m}$ image but the top spectrum along the $+8^\circ$ slit is significantly to the west of the knot. In the bottom panel, the silicate absorption remains strong and the flux rises in the short wavelength end like in CE. In contrast, the top panel shows that the silicate absorption is weak and the spectrum is flat. The centers of the silicate absorption lines appear blue-shifted. The relative [S IV] emission lines appear stronger than both at the CE and South 1 in both panels.

A.8. Mid-IR spectra at South 3

Figure 15, South 3, depicts the spectra of NGC 1068 at $0.75''$ south of the central peak along the $+8^\circ$ slit in the top panel and the -13° slit in the bottom panel. This position is below the lowest contour in the $12\ \mu\text{m}$ image, and both spectra are noisy and the flux drops to 2% of the CE. In the top panel, the spectrum is very red and shows little silicate absorption. In the bottom panel, however, the spectrum is flat and displays strong silicate absorption. The relative [S IV] emission lines have higher equivalent width than in South 2.

REFERENCES

- Antonucci, R. 1993, *ARA&A*, 31, 473
- Antonucci, R. R. J., & Miller, J. S. 1985, *ApJ*, 297, 621
- Bock, J. J., Neugebauer, G., Matthews, K., Soifer, B. T., Becklin, E. E., Ressler, M., Marsh, K., Werner, M. W., Egami, E., & Blandford, R. 2000, *AJ*, 120, 2904
- Braatz, J. A., Wilson, A. S., Gezari, D. Y., Varosi, F., & Beichman, C. A. 1993, *ApJ*, 409, 5
- Cameron, M., Storey, J. W. V., Rotaciuc, V., Genzel, R., Verstraete, L., Drapatz, S., Siebenmorgen, R., & Lee, T. J. 1993, *ApJ*, 419, 136
- Clavel, J., Schulz, B., Altieri, B., Barr, P., Claes, P., Heras, A., Leech, K., Metcalfe, L., & Salama, A. 2000, *A&A*, 257, 839
- Dudley, C. C., & Wynn-williams, C. G. 1997, *ApJ*, 488, 720
- Evans, I. N., Ford, H. C., Kinney, A. L., Antonucci, R. R. J., Armus, L., & Caganoff, S. 1991, *ApJ*, 369, L27
- Galliano, E., Alloin, D., Granato, G. L., & Villar-Martin, M. 2003, *A&A*, 412, 615
- Gallimore, J. A., Baum, S. A., & O’Dea, C. P. 1996, *ApJ*, 464, 198
- Gorjian, V., Werner, M. W., Jarret, T. H., Cole, D. M., & Ressler, M. E. 2004, *ApJ*, 605, 156
- Granato, G. L., & Danese, L. 1994, *MNRAS*, 268, 235
- Granato, G. L., Danese, L., & Franceschini, A. 1997, *ApJ*, 486, 147
- Jaffe, W., Meisenheimer, K., Rottgering, H. J. A., et al. 2004, *Nature*, 429, 47
- Jones, B., & Puetter, R. 1993, *Proc. SPIE*, 1946, 610
- Le Floc’h, E., Mirabel, I. F., Laurent, O., Charmandaris, V., Gallais, P., Sauvage, M., Vigroux, L., & Cesarsky, C. 2001, *A&A*, 367, 487
- lord, S. D. 1992, *NASA Technical Memor.* 103957
- Lutz, E., Sturm, E., Genzel, R., Moorwood, A. F. M., Alexander, T., Netzer, H., & Sternberg, A. 2000, *ApJ*, 536, 697

- Macchetto, F., Capetti, A., Sparks, W. B., Axon, D. J., & Boksenberg, A. 1994, *ApJ*, 435, L15
- Maiolino, R., Marconi, A., Salvati, M., Risaliti, G., Severgnini, P., Oliva, E., La Franca, F., & Vanzi, L. 2001, *A&A*, 365, 28
- Nenkova, M., Ivezić, Z., & Elitzer, M. 2002, *ApJ*, 570, L9
- Pier, E., & Krolik, J. 1992, *ApJ*, 401, 99
- Pier, E., & Krolik, J. 1993, *ApJ*, 418, 673
- Rhee, J. H., & Larkin, J. E. 2005, *ApJ*, 620, 151
- Rieke, G. H., & Low, F. J. 1975, *ApJ*, 199, L13
- Roche, P. F., & Aitken, D. K. 1984, *MNRAS*, 208, 481
- Roche, P. F., Aitken, D. K., Smith, C. H., & Martin, J. W. 1991, *MNRAS*, 248, 606
- Rowan-Robinson, M. 1995, *MNRAS*, 272, 737
- Siebenmorgen, R., Krugel, E., & Spoon, H. W. W. 2004, *A&A*, 414, 123
- Soifer, T. B., Neugebauer, G., Matthews, K., & Egami, E. 2002, *AJ*, 12, 2980
- Sturm, E., Lutz, D., Tran, D., Feuchtgruber, H., Genzel, R., Kunze, D., Moorwood, A. F. M., & Thornley, M. D. 2000, *A&A*, 358, 481
- Tomono, D., Doi, Y., Usuda, T., Nishimura, T. 2001, *ApJ*, 557, 637
- Tully, R. B. 1988, *Nearby Galaxies Catalog*(New York: Cambridge Univ. Press)
- Weingartner, J. C. & Murray, N. 2001, *ApJ*, 88, 95

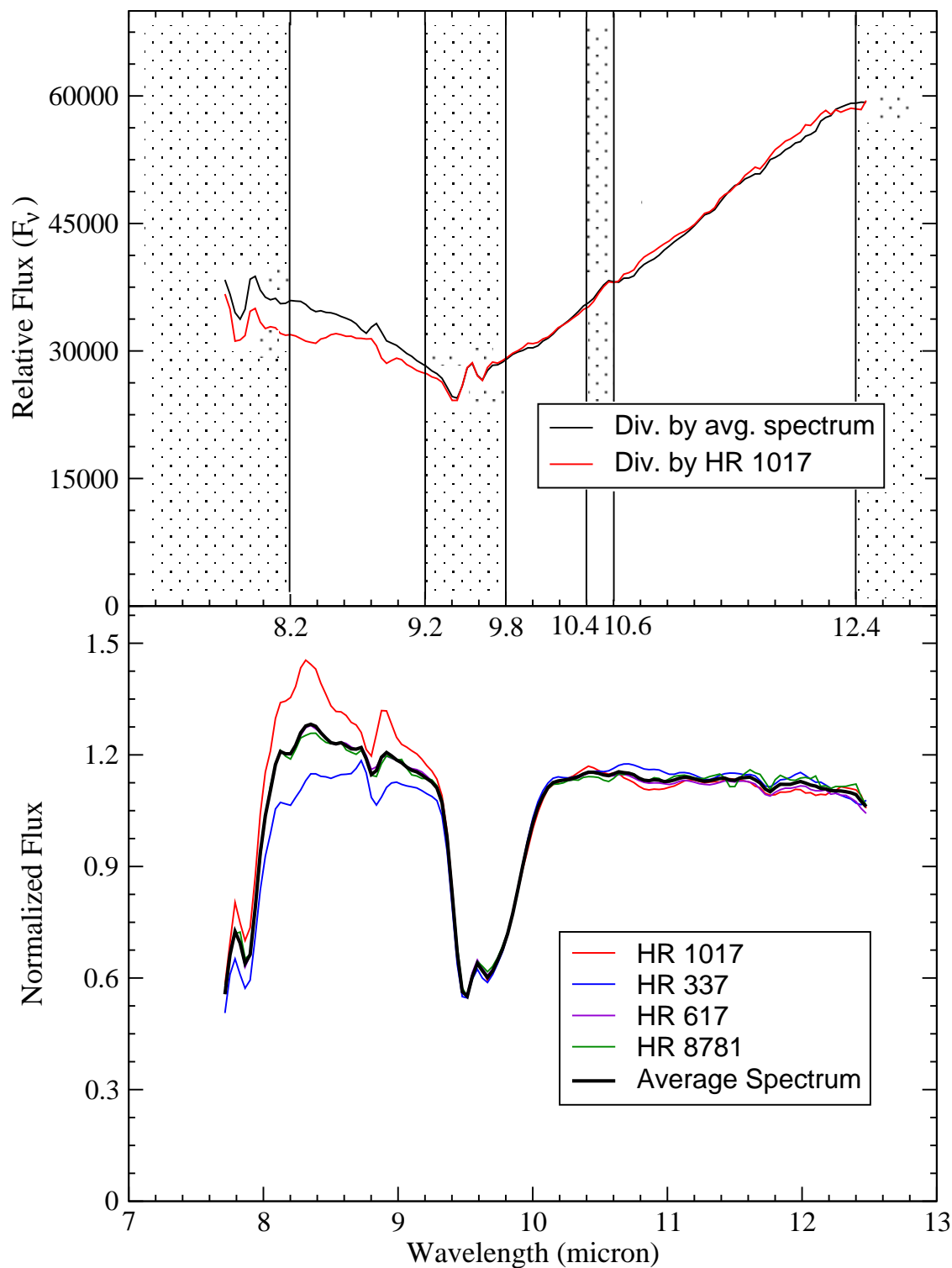


Fig. 1.— Calibration of the mid-IR spectra of NGC 1068. The top panel shows two mid-IR spectra of NGC 1068 at the nucleus: one (black line) divided by the average spectrum of 4 standard stars and the other (red line) divided by the spectrum of HR 1017. The bottom panel displays spectra of all 4 standard stars. When divided by the spectrum of HR 1017, the mid-IR spectrum of NGC 1068 produces unknown broad emission-like features between 8.4 and 8.8 microns. The shaded regions in the top panel indicate the wavelength regions omitted from the fitting process.

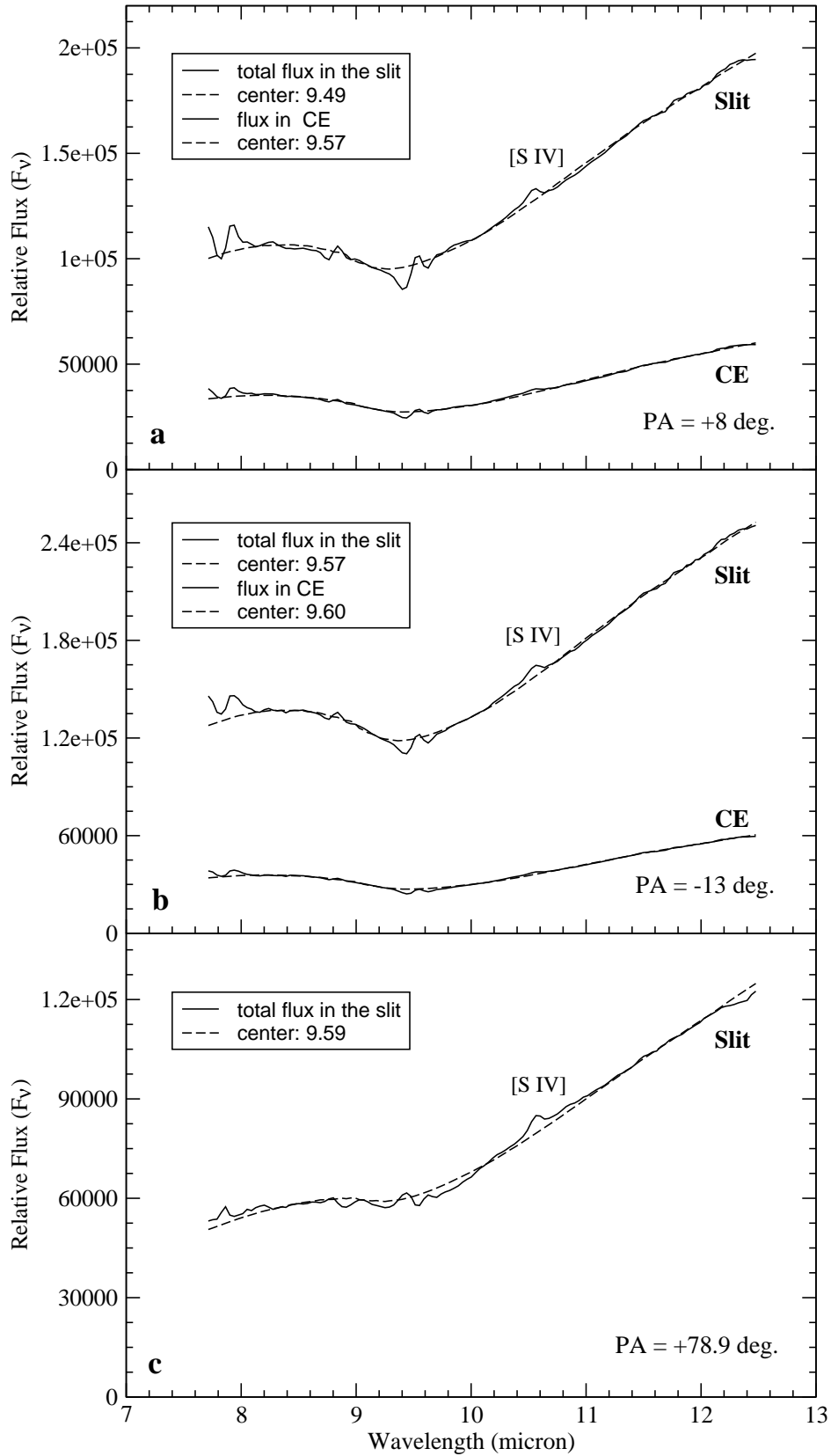


Fig. 2.— Mid-infrared spectra of NGC 1068 along +8°, -13°, and -78.9° slits. The continuum is fit with a silicate extinction curve shown as a dashed line.

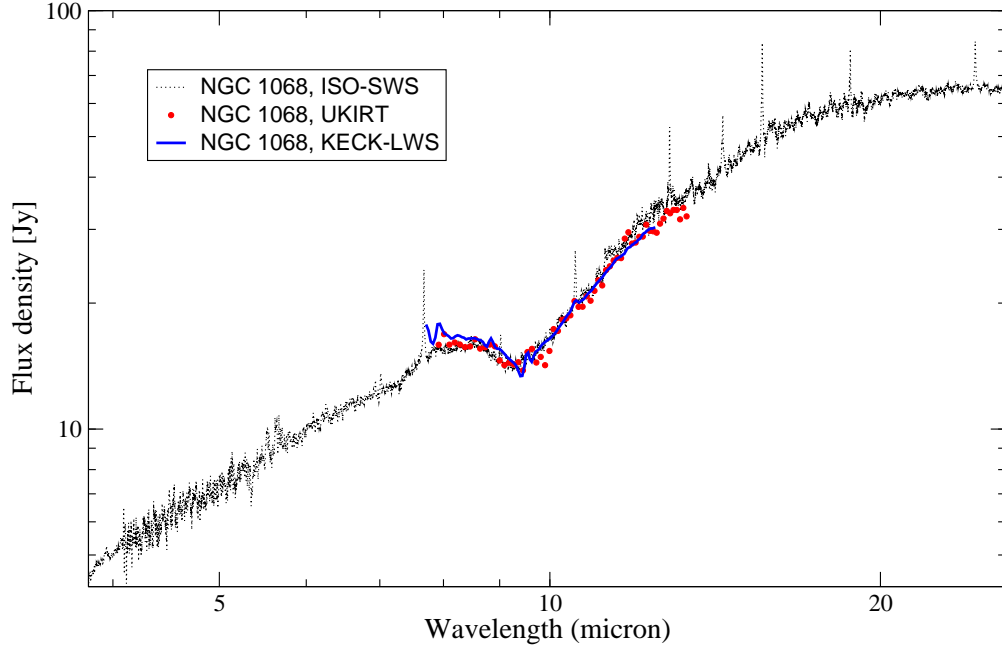


Fig. 3.— The mid-IR spectra of NGC 1068. The Keck LWS mid-infrared spectrum of NGC 1068 was created by averaging two spectra along $+8^\circ$ and -13° slits and scaling to match the ISO-SWS spectrum. The UKIRT spectrum is a reproduction of the mid-infrared spectrum of NGC 1068 in Figure 1 from Roche et al. (1991). λF_λ was first converted to F_ν and then scaled to match the ISO-SWS spectrum. Dr. Roche kindly provided his UKIRT data for this Figure. The LWS spectrum ($0.25'' \times 2''$) matches ISO-SWS spectrum ($12'' \times 20''$ for short wavelength and $20'' \times 33''$ for long wavelength) and UKIRT spectrum ($5''$ circular aperture) quite well, especially the depth of the silicate absorption. A better spatial resolution of NGC 1068 resulted from its proximity may explain that the AGN dominates the mid-IR flux of NGC 1068 in these spectra. D. Lutz kindly provided the ISO-SWS data that were used for Figure 1 in Lutz et al. (2000)

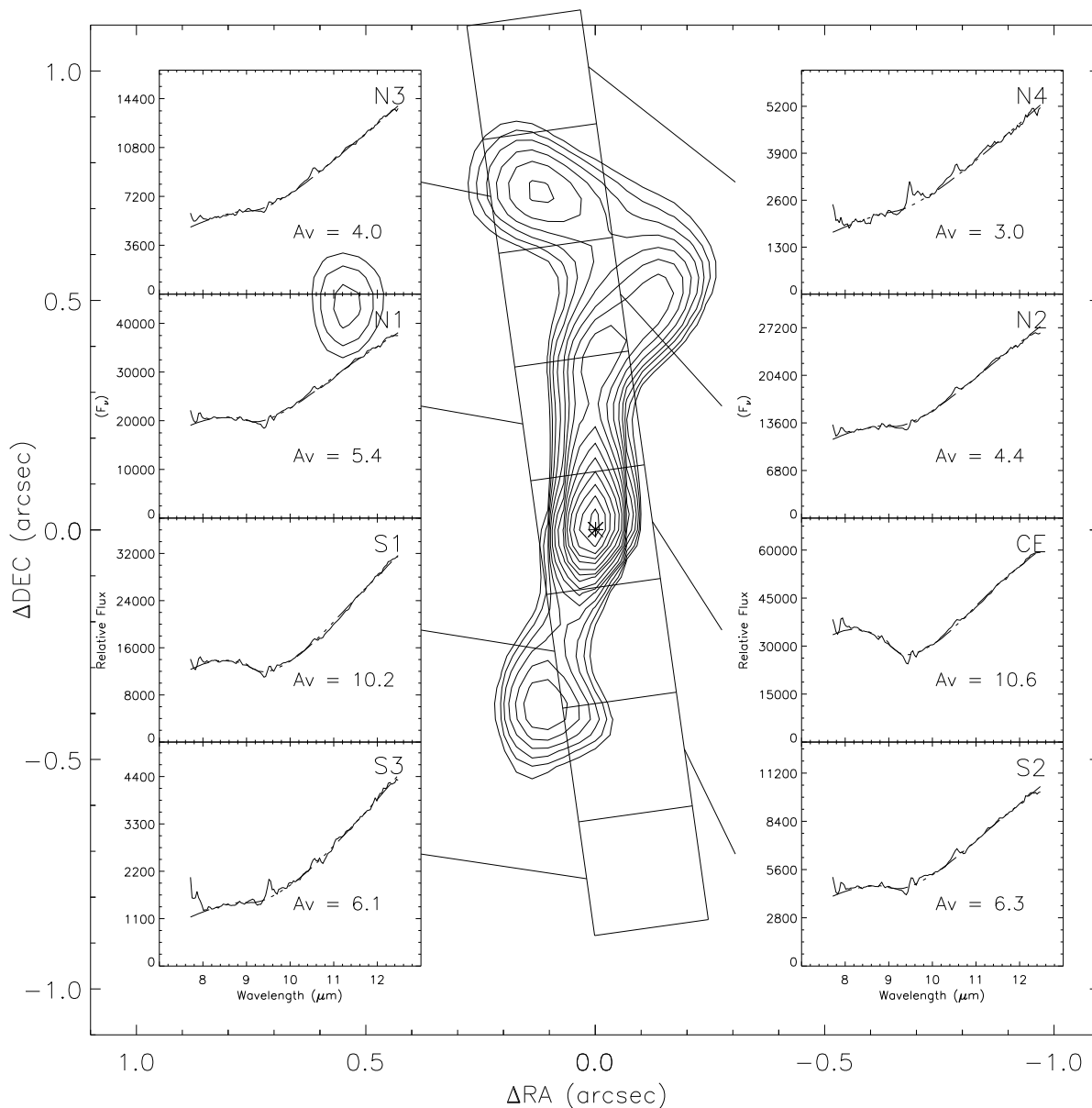


Fig. 4.— Mid-infrared spectra of NGC 1068 along $+8^\circ$ slit overlaid on $12\ \mu\text{m}$ deconvolved image of NGC 1068 from Bock et al. (2000). Each spectrum is produced from a $0.25'' \times 0.25''$ square beam and plotted in Relative Flux (F_ν) as a function of wavelength (μm). In each set, the continuum is fit with a silicate extinction curve shown as a dashed line.

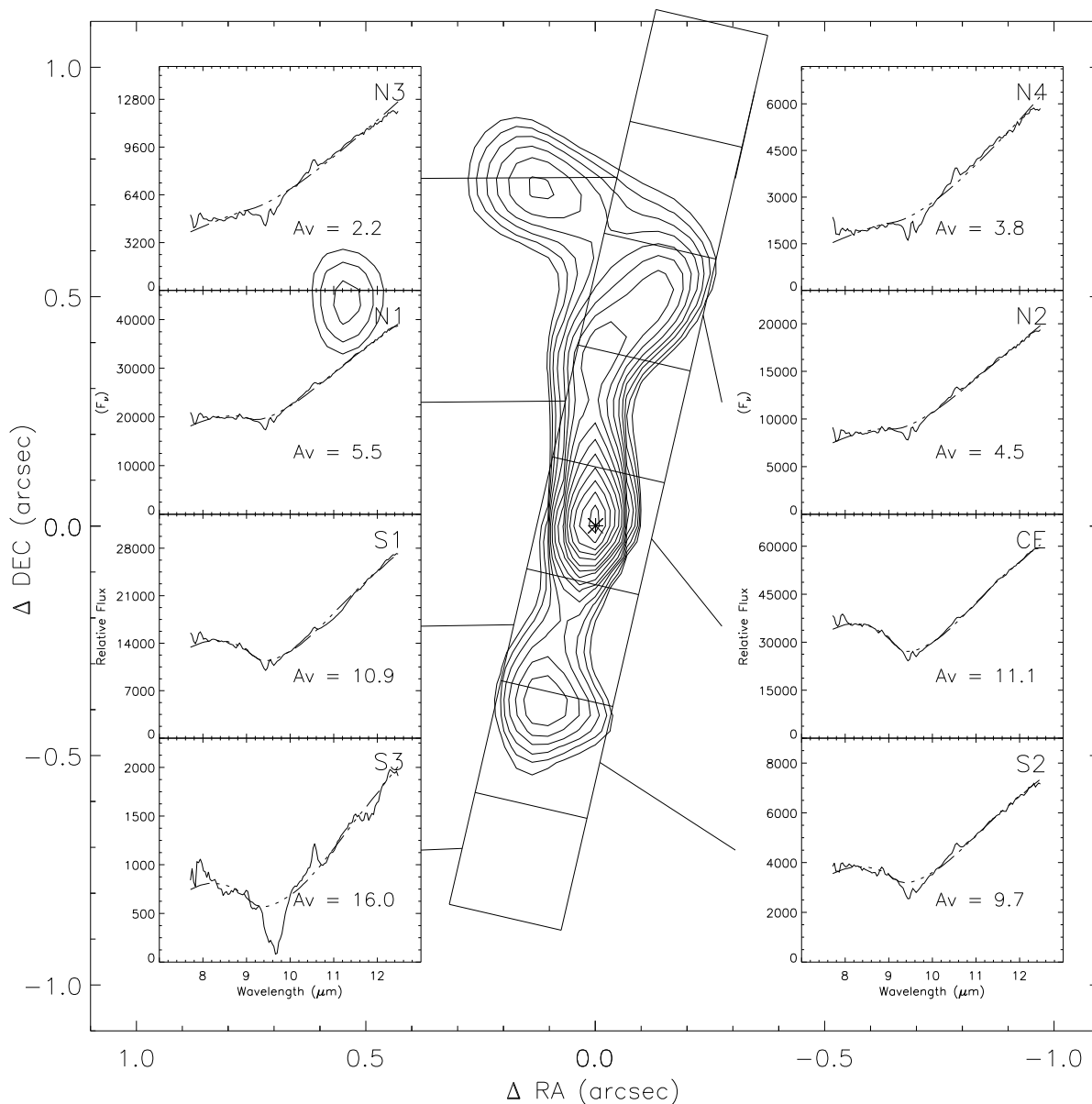


Fig. 5.— Mid-infrared spectra of NGC 1068 along -13° slit overlaid on $12\ \mu\text{m}$ deconvolved image of NGC 1068 from Bock et al. (2000). Each spectrum is produced from a $0.25'' \times 0.25''$ square beam and plotted in Relative Flux (F_ν) as a function of wavelength (μm). In each set, the continuum is fit with a silicate extinction curve shown as a dashed line.

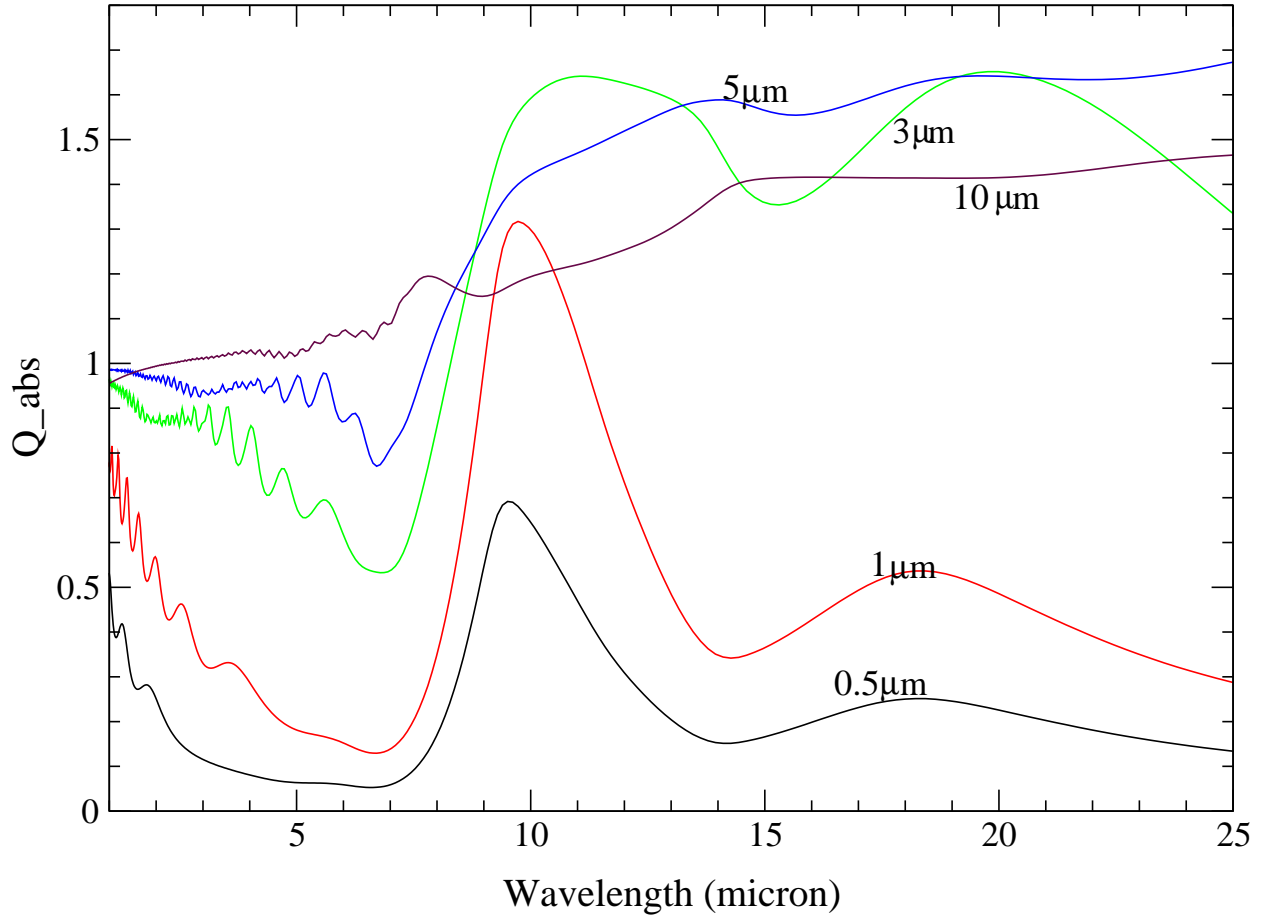


Fig. 6.— Absorption efficiency of silicate grains vs. its size. This figure is produced using a code used in Figure 5 in Draine and Lee (1984). Aigen Li kindly provided the code for this paper.

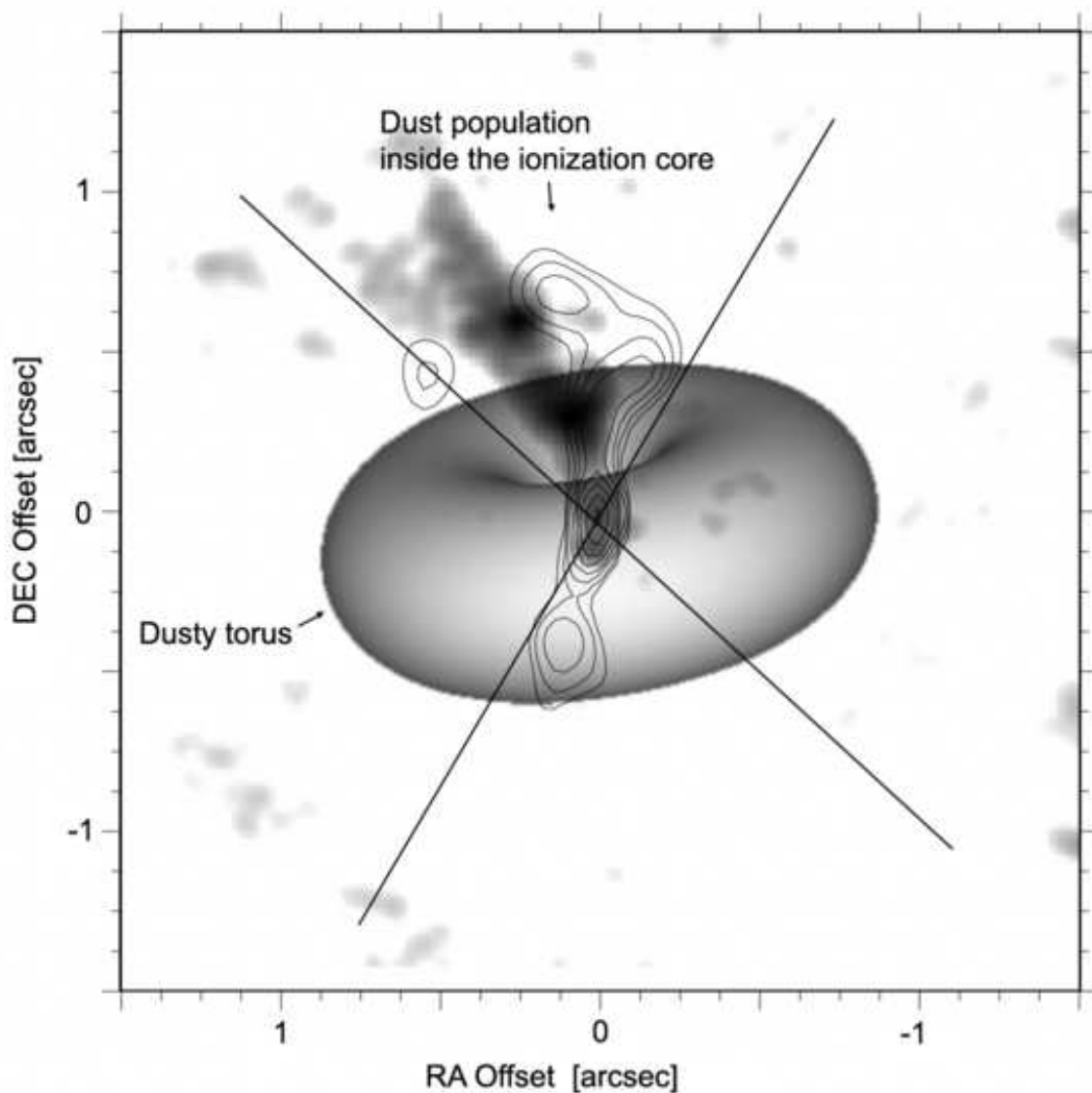


Fig. 7.— Dual dust populations in the nuclear environment of NGC 1068: one inside the ionization cone and the other in the form of a torus. The small grains are depleted in the dust clouds inside the ionization cone giving rise to nearly flat mid-ir spectra in the northern extended regions. But these grains are present in the torus and produce strong $9.7 \mu\text{m}$ silicate absorption. The background image of NGC 1068 was taken from Figure 4 in Bock et al. (2000) in which the contour plot of the $12.5 \mu\text{m}$ image was superimposed on the 5 GHz map of Gallimore et al. (1996). The size and shape of the dusty torus in the figure does not necessarily depict the true torus as this could not be determined by our data.

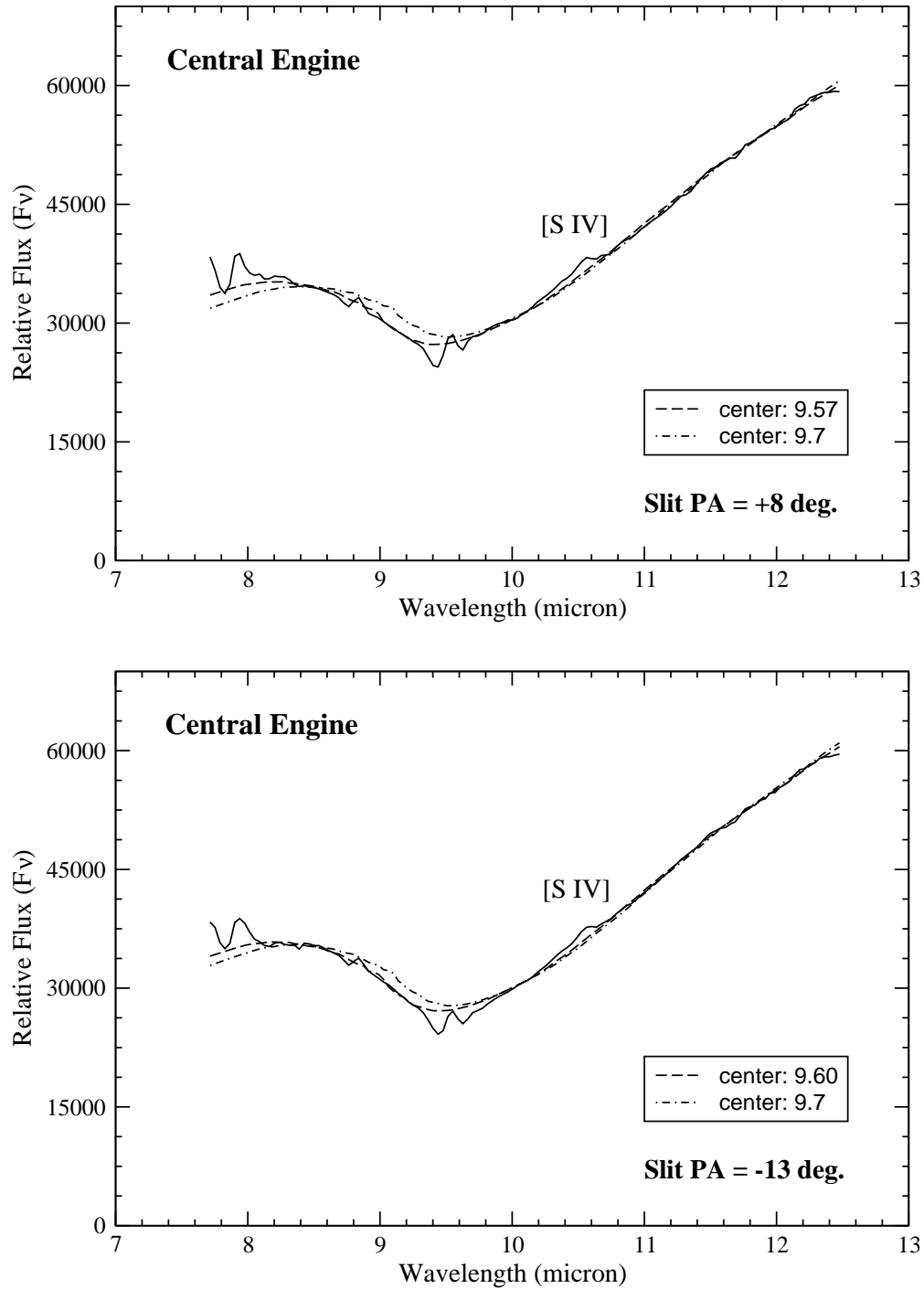


Fig. 8.— Central Engine: Mid-infrared spectra of NGC 1068. The top panel is from the slit along $+8^\circ$ and the bottom panel from -13° . Each spectrum is produced from a $0.25'' \times 0.25''$ square beam. In each set, the observed spectrum is fit with the silicate extinction curve. A dashed line represents the best fit and a dashed-dotted line the fit with a center at $9.7 \mu\text{m}$.

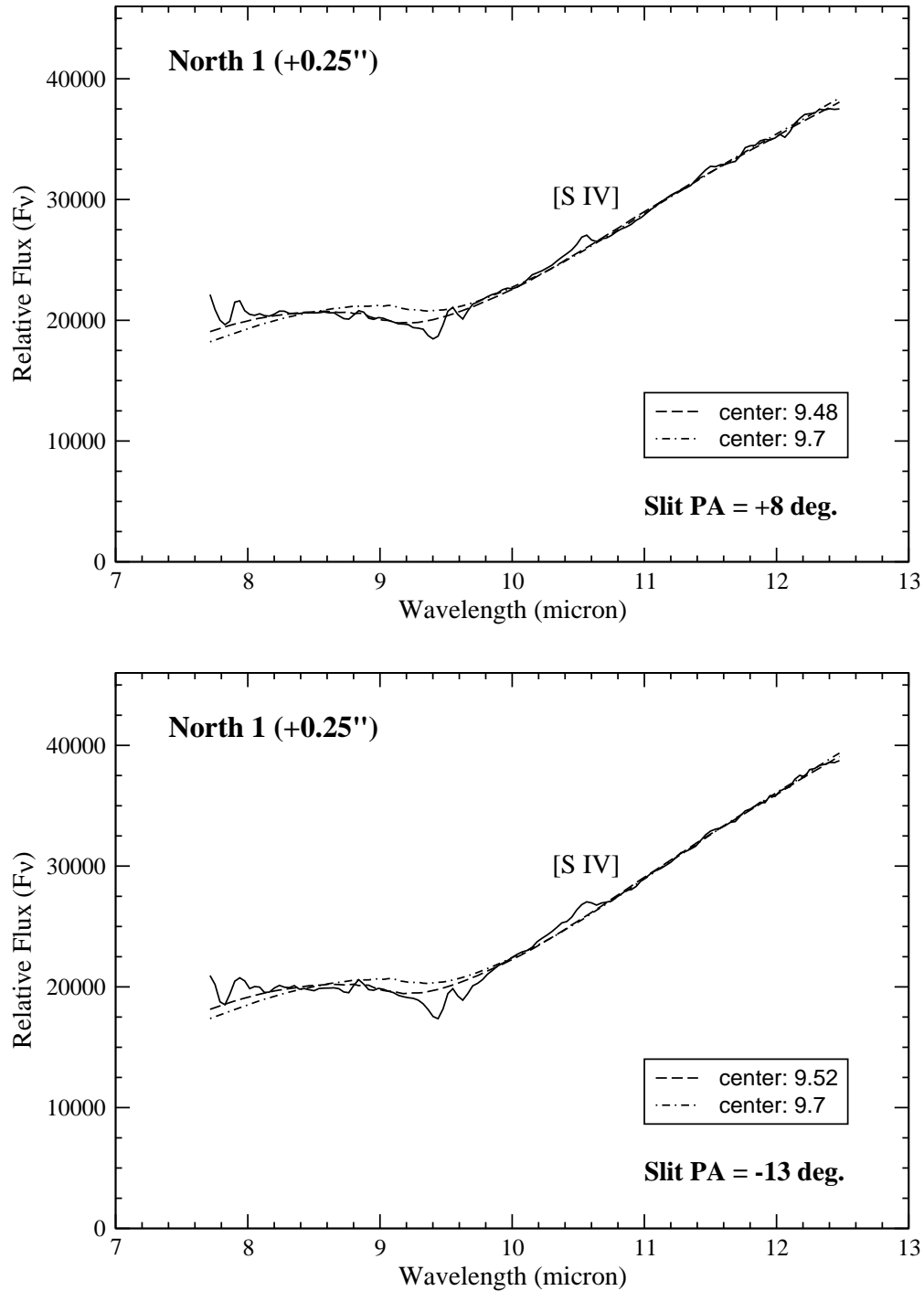


Fig. 9.— North 1: Mid-infrared spectra of NGC 1068. The top panel is from the slit along $+8^\circ$ and the bottom panel from -13° . Each spectrum is produced from a $0.25'' \times 0.25''$ square beam. In each set, the observed spectrum is fit with the silicate extinction curve. A dashed line represents the best fit and a dashed-dotted line the fit with a center at $9.7 \mu\text{m}$.

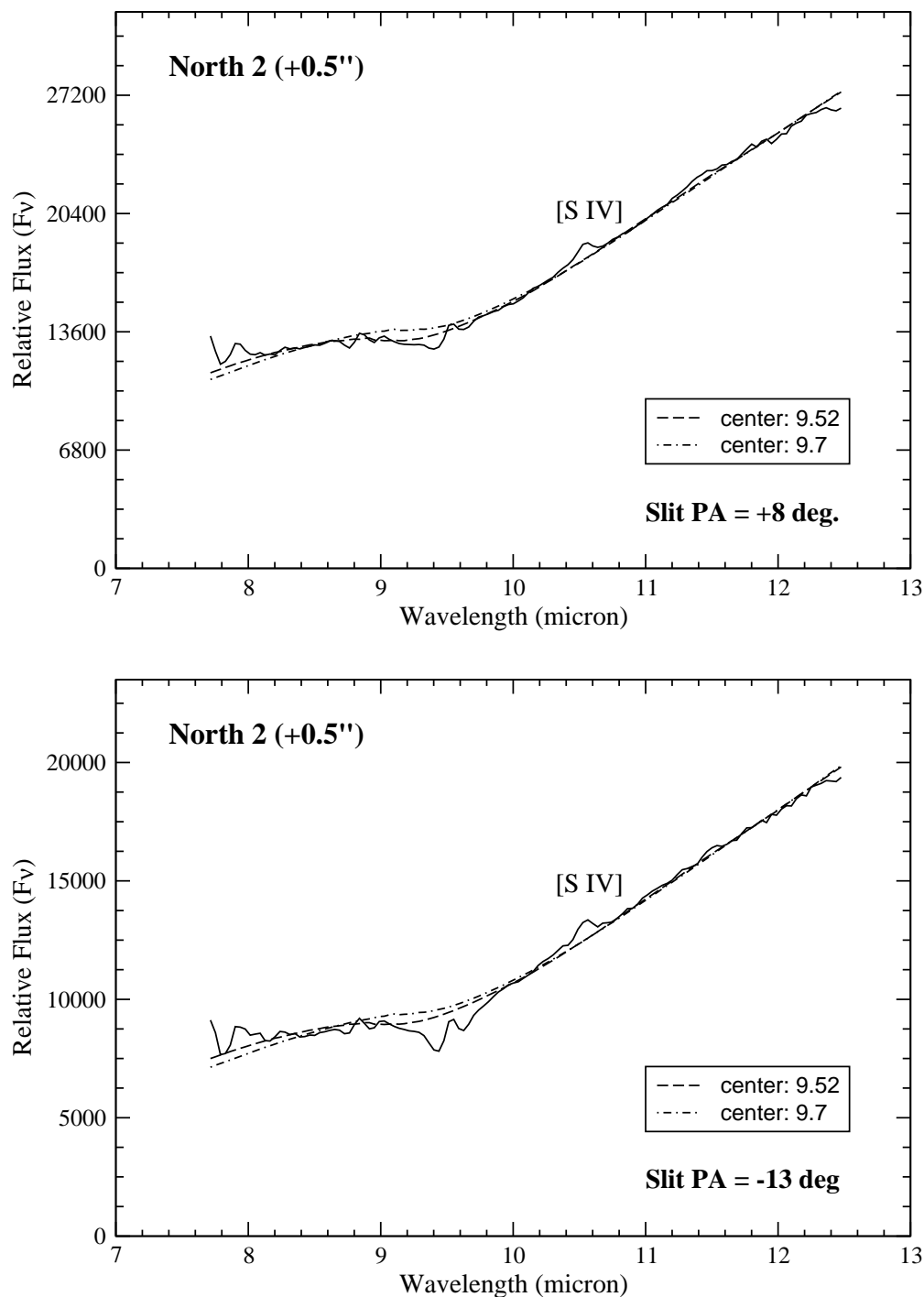


Fig. 10.— North 2: Mid-infrared spectra of NGC 1068. The top panel is from the slit along $+8^\circ$ and the bottom panel from -13° . Each spectrum is produced from a $0.25'' \times 0.25''$ square beam. In each set, the observed spectrum is fit with the silicate extinction curve. A dashed line represents the best fit and a dashed-dotted line the fit with a center at $9.7 \mu\text{m}$.

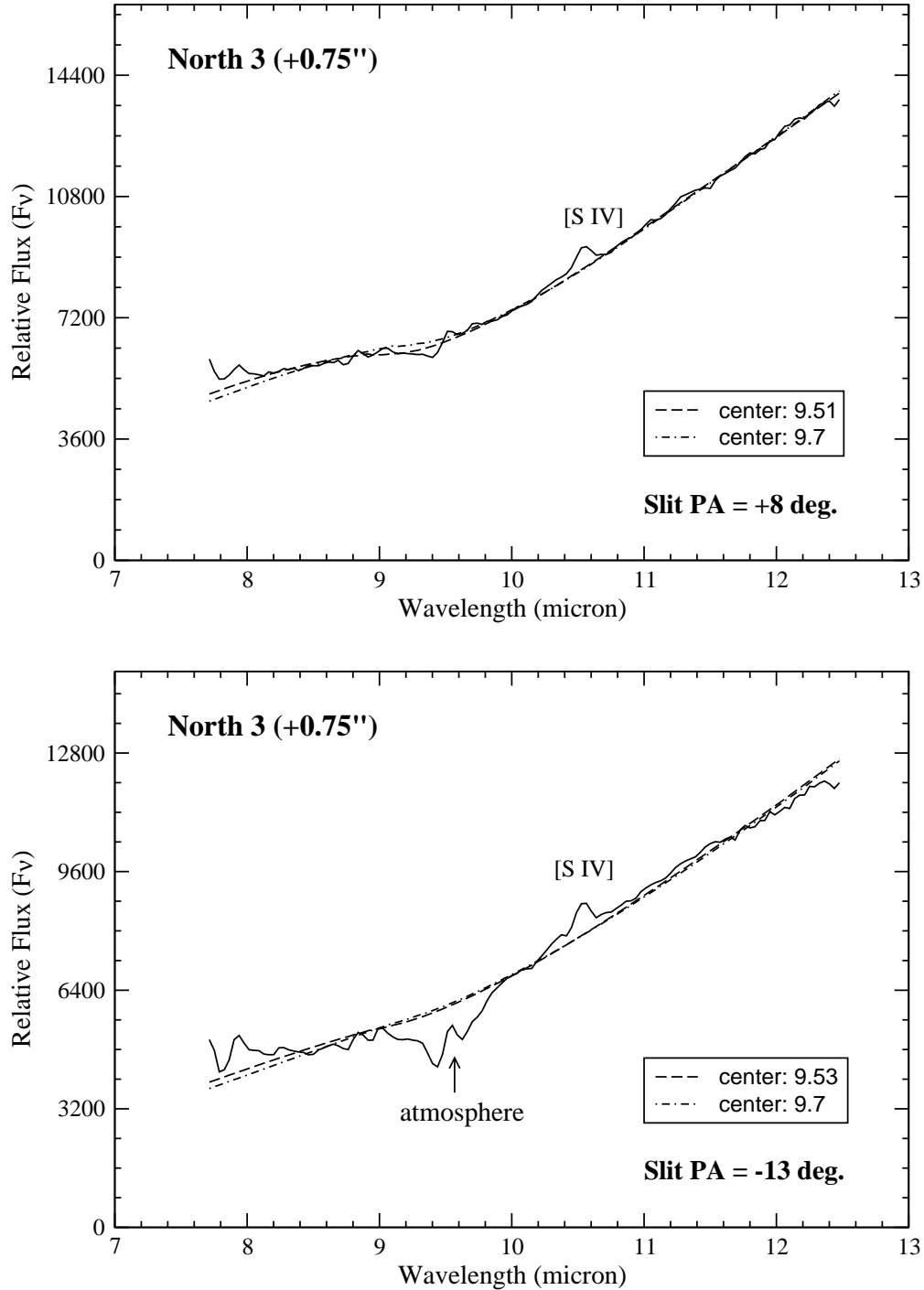


Fig. 11.— North 3: Mid-infrared spectra of NGC 1068. The top panel is from the slit along $+8^\circ$ and the bottom panel from -13° . Each spectrum is produced from a $0.25'' \times 0.25''$ square beam. In each set, the observed spectrum is fit with the silicate extinction curve. A dashed line represents the best fit and a dashed-dotted line the fit with a center at $9.7 \mu\text{m}$.

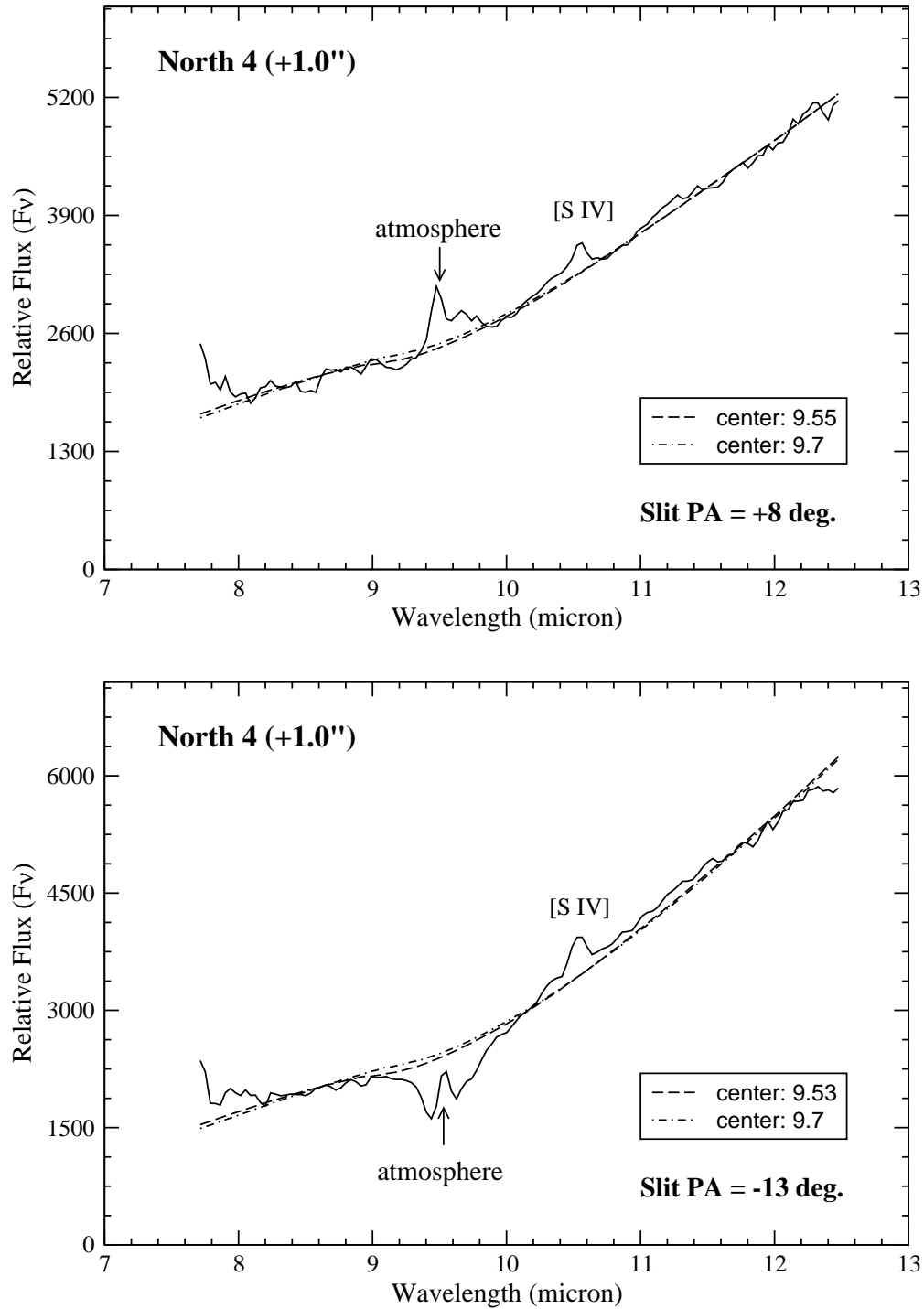


Fig. 12.— North 4: Mid-infrared spectra of NGC 1068. The top panel is from the slit along $+8^\circ$ and the bottom panel from -13° . Each spectrum is produced from a $0.25'' \times 0.25''$ square beam. In each set, the observed spectrum is fit with the silicate extinction curve. A dashed line represents the best fit and a dashed-dotted line the fit with a center at $9.7 \mu\text{m}$.

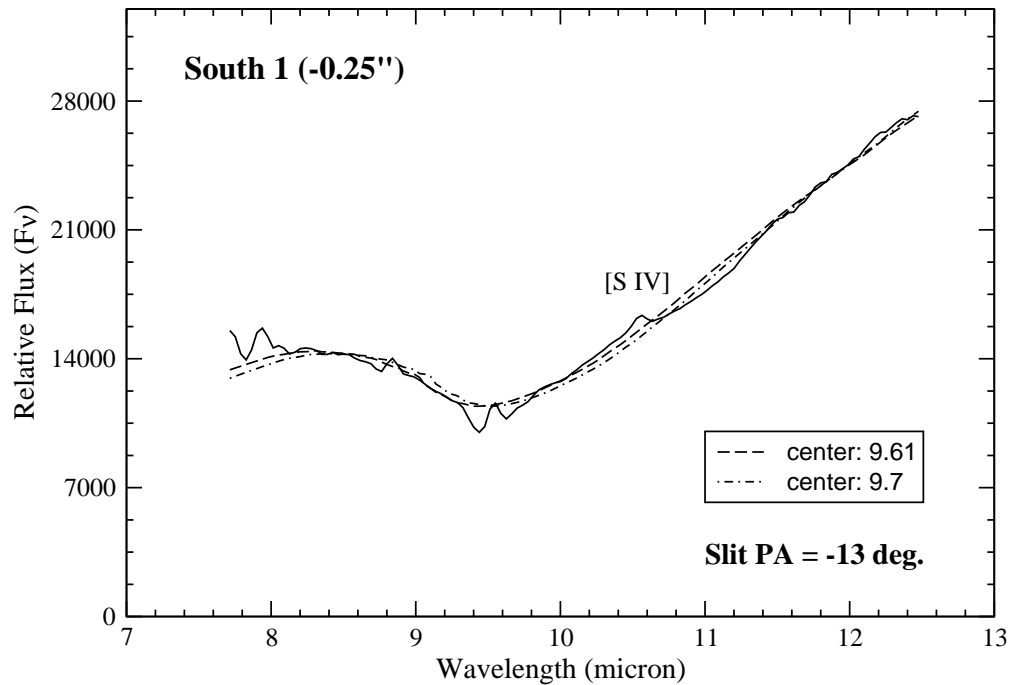
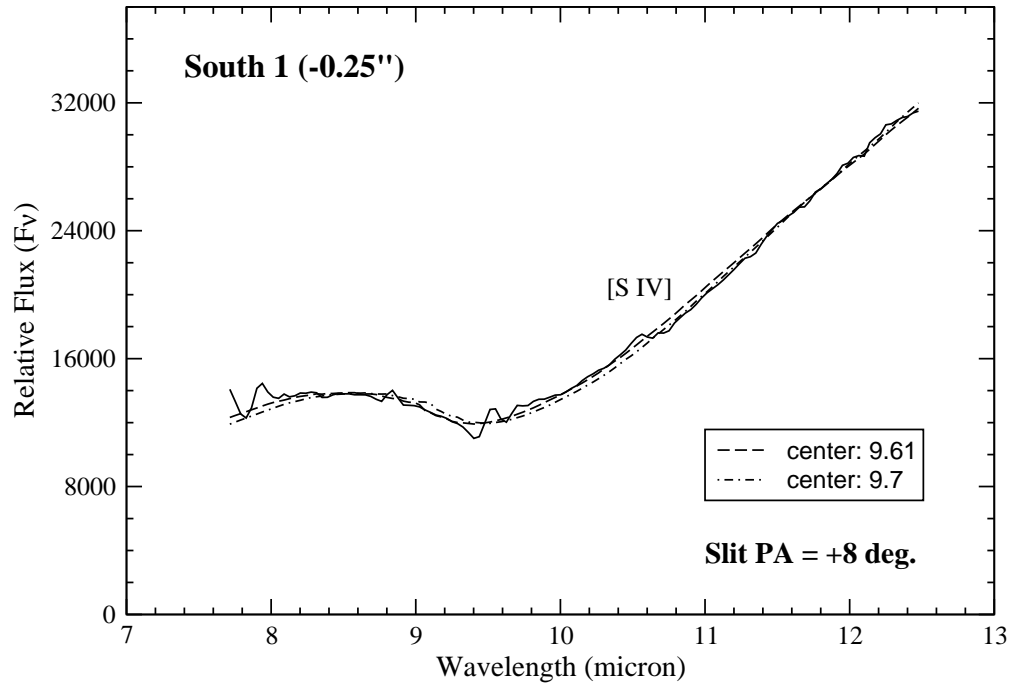


Fig. 13.— South 1: Mid-infrared spectra of NGC 1068. The top panel is from the slit along $+8^\circ$ and the bottom panel from -13° . Each spectrum is produced from a $0.25'' \times 0.25''$ square beam. In each set, the observed spectrum is fit with the silicate extinction curve. A dashed line represents the best fit and a dashed-dotted line the fit with a center at $9.7 \mu\text{m}$.

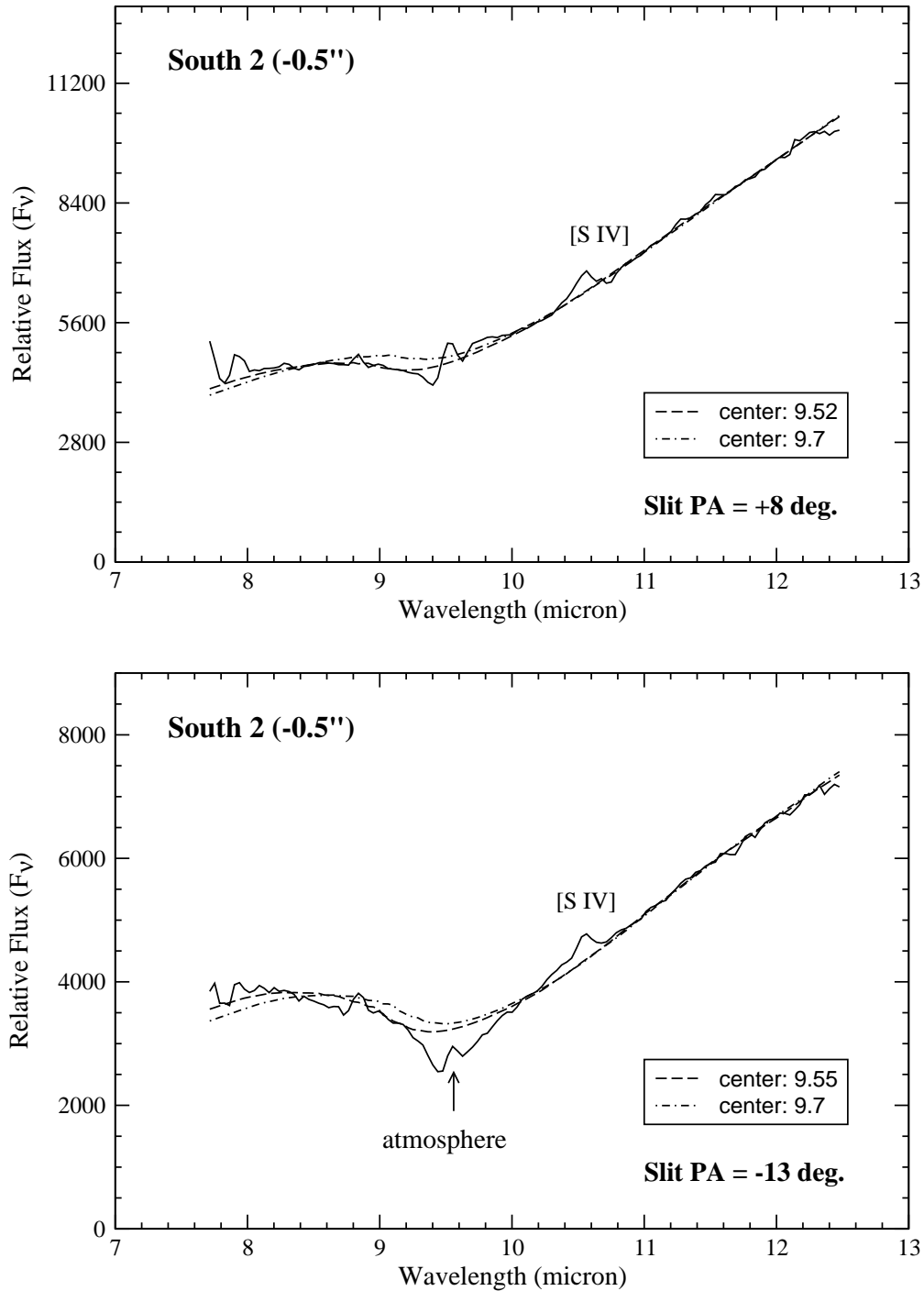


Fig. 14.— South 2: Mid-infrared spectra of NGC 1068. The top panel is from the slit along $+8^\circ$ and the bottom panel from -13° . Each spectrum is produced from a $0.25'' \times 0.25''$ square beam. In each set, the observed spectrum is fit with the silicate extinction curve. A dashed line represents the best fit and a dashed-dotted line the fit with a center at $9.7 \mu\text{m}$.

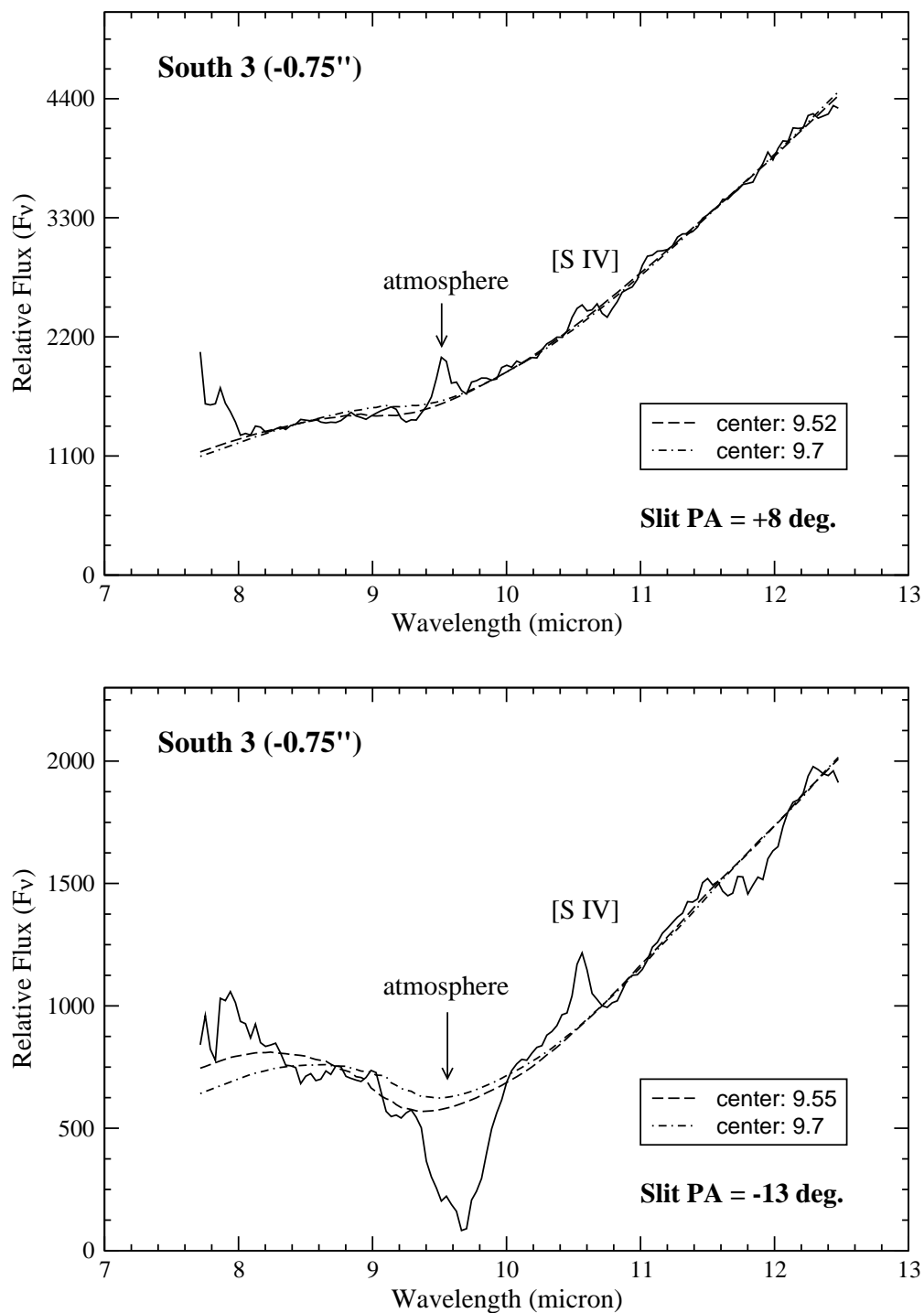


Fig. 15.— South 3: Mid-infrared spectra of NGC 1068. The top panel is from the slit along $+8^\circ$ and the bottom panel from -13° . Each spectrum is produced from a $0.25'' \times 0.25''$ square beam. In each set, the observed spectrum is fit with the silicate extinction curve. A dashed line represents the best fit and a dashed-dotted line the fit with a center at $9.7 \mu\text{m}$.

Table 1. OBSERVATION SUMMARY

Object	Slit PA(°)	Type	cz	airmass ^a	Total Integration ^b Time(sec)	Date of Observation
NGC 1068	+8	S1.8	1.003793	1.06	504	2003 Sep
NGC 1068	+78.9	S1.8	1.003793	1.10	504	2003 Sep
NGC 1068	-13	S1.8	1.003793	1.07	504	2003 Sep

^aaverage for all three runtime sets at each slit position.

^bfor all three runtime sets. Intergration time for each runtime set is 168 seconds.

Table 2. SPATIALLY RESOLVED 9.7 μm SILICATE FEATURE IN NGC 1068

Location	Slit PA	Fitting Parameters			
		Center(μm)	Index ^a	A_v	χ^2/N
North 4	+8°	9.55	2.35	2.98	1.19
	-13°	9.53	2.95	3.83	1.25
North 3	+8°	9.51	2.18	4.01	1.11
	-13°	9.53	2.55	2.17	1.33
North 2	+8°	9.52	1.88	4.44	1.05
	-13°	9.52	2.05	4.46	1.31
North 1	+8°	9.48	1.47	5.42	1.42
	-13°	9.52	1.63	5.47	1.73
Central	+8°	9.57	1.29	10.59	1.16
Engine	-13°	9.60	1.28	11.12	0.98
South 1	+8°	9.61	2.05	10.20	1.27
	-13°	9.61	1.56	10.90	1.54
South 2	+8°	9.52	2.01	6.34	0.92
	-13°	9.58	1.58	9.72	1.10
South 3	+8°	9.52	2.87	6.10	0.81
	-13°	9.55	2.12	15.98	1.80

^aThe power-law index, α , for $F_\nu \sim \nu^{-\alpha}$.